This is a peer-reviewed, accepted author manuscript of the following research article: Suryasentana, SK, Sheil, BB & Stuyts, B 2024, 'Multifidelity data fusion for the estimation of static stiffness of suction caisson foundations in layered soil', Journal of Geotechnical and Geoenvironmental Engineering, vol. 150, no. 8. https://doi.org/10.1061/jggefk.gteng-11819

Multi-fidelity data fusion for the estimation of static stiffness of suction caisson foundations in layered soil

Stephen K. Suryasentana[1], Ph.D.
Brian B. Sheil[2], Ph.D.
Bruno Stuyts[3,4], MSc.

Affiliations

[1] Lecturer, Department of Civil and Environmental Engineering, University of Strathclyde, 75 Montrose St, Glasgow G1 1XJ, UK.

[2] Laing O'Rourke Associate Professor in Construction Engineering, Department of Engineering, University of Cambridge, Trumpington St, Cambridge CB2 1PZ, UK.

[3] Doctoral researcher, OWI-Lab, Vrije Universiteit Brussel, Pleinlaan 2, Elsene,1050 Brussels, Belgium.

[4] Visiting Professor, Geotechnical Laboratory, Ghent University, Technologiepark 68 B-9052 Gent, Belgium.

Full contact details of corresponding author

Stephen K. Suryasentana

stephen.suryasentana@strath.ac.uk

Main text word count: 5588

Figures: 13

Tables: 3

Feb 17, 2023

Abstract

The static stiffness of suction caisson foundations is an important engineering factor for offshore wind foundation design. However, existing simplified design models are mainly developed for non-layered soil conditions, and their accuracy for layered soil conditions is uncertain. This creates a challenge for designing these foundations in offshore wind farm sites, where layered soil conditions are commonplace. To address this, this paper proposes a multi-fidelity data fusion approach that combines information from different physics-based models of varying accuracy, data sparsity and computational costs in order to improve the accuracy of stiffness estimations for layered soil conditions. The results indicate that the proposed approach is more accurate than both the simplified design model and a single-fidelity machine learning model, even with limited training data. The proposed method offers a promising data-efficient solution for fast and robust stiffness estimations, which could lead to more cost-effective offshore foundation designs.

Keywords
machine learning, shallow foundations, soil-structure interaction

Introduction

Offshore wind energy is a crucial component in the global effort to decarbonize energy systems in Europe, Asia, and America (Diaz and Soares 2020). To meet the increasing demand for offshore wind energy, offshore wind farms are expected to expand into deeper waters, where wind resources are more abundant. Suction caisson foundations are an important foundation option for offshore wind turbines in deeper waters (Byrne and Houlsby 2003). They can be used as jacket-based foundations in transitional waters (30m-60m water depth) or as anchors for floating wind mooring systems in deep waters.

The geotechnical design of suction caisson foundations for offshore wind applications requires several key design considerations (Sturm 2017), including estimations of foundation capacity (e.g., Samui et al. 2011; Liu et al. 2014; Bagheri et al. 2017; Barari et al. 2017; Wang and Cheng 2016; Ukritchon and Keawsawasvong 2016; Yang et al. 2018; Nielsen 2019; Gelagoti et al. 2019; He at el. 2021; Wang et al. 2022; Wu et al. 2022; Liu et al. 2023) for ultimate limit state assessments, installation analysis (e.g., Houlsby and Byrne 2005a, b; Anderson et al. 2008; Senders and Randolph 2009), estimations of displacements and tilt under monotonic loading (e.g., Suryasentana et al. 2018, 2019, 2023b), seismic loading (e.g., Kourkoulis et al. 2014; Esfeh and Kaynia 2020; Antoniou et al. 2022) and cyclic loading (e.g., Foglia et al. 2014; Skau et al. 2018, 2019; Zhu et al. 2018, 2019; Byrne et al. 2020; Yin et al. 2020) for serviceability limit state assessments, and estimation of the stiffness of the caisson response for natural frequency and fatigue limit state assessments. Previous studies (e.g., Latini and Zania 2017; Jalbi et al. 2019) have shown that the dynamic stiffness of the caisson response affects the eigenfrequency of vibration of the offshore wind support structures and thus, their fatigue life.

This paper focuses on the estimation of the static stiffness of the caisson response, which are key inputs for the estimation of the dynamic stiffness of the caisson response. Efficient design models are essential for large-scale foundation projects like offshore wind farms, where hundreds of foundations must be optimized. However, existing efficient, simplified design models or empirical formulae (e.g., Suryasentana et al. 2017, 2022, Doherty et al. 2005; Efthymiou and Gazetas 2018; Skau et al. 2019; Jalbi et al. 2018; Gelagoti et al. 2018) have mostly been developed to estimate the static stiffness of caisson response for specific, non-

layered, homogeneous or non-homogeneous shear modulus profiles that conform to some parametric form (e.g., constant, linearly or non-linearly increasing with depth). They have not been validated for layered soil conditions typically encountered in offshore wind farm sites (Burd et al. 2020), and their accuracy in predicting the caisson response in layered soil conditions, particularly those with high stiffness contrasts between each soil layer, is uncertain.

For complex soil conditions, such as interbedded layered soil conditions, three-dimensional (3D) finite element analysis (FEA) may be necessary to estimate the static stiffness accurately. Unfortunately, 3D FEA is computationally intensive and not practical for wind farm foundation design optimization, which requires a large number of low-cost calculations to optimize the sizing of hundreds of foundations in varying ground conditions and different potential wind farm layout configurations, especially during the preliminary design stage.

Metamodelling, also known as surrogate modelling, has been proposed as a technique to reduce FEA computational costs for offshore pile design (Mentani et al. 2023) and suction caisson design (Yin et al. 2023). This approach allows fast approximation of the FEA results using machine learning techniques such as polynomial chaos expansion (Mentani et al. 2023), radial basis functions (Wang and Owens 2022), artificial neural networks (Shen et al. 2022) and kriging (Kang et al. 2015, Soubra et al. 2019). However, metamodels usually require large training datasets (Mentani et al. 2023), which limits their applicability when FEA data is scarce.

To overcome this limitation, multi-fidelity data fusion (MFDF) has emerged as an effective solution, particularly in aerospace engineering for tasks like space vehicle design (Minisci et al. 2011). MFDF combines information from multiple datasets of different accuracy and volume to improve predictive accuracy. It leverages both low-fidelity data from simplified models and high-fidelity data from detailed, computationally intensive simulations like 3D FEA. The fusion of these datasets allows MFDF to achieve greater predictive accuracy while requiring significantly less high-fidelity data compared to traditional metamodeling (Meng and Karniadakis 2020). This method is especially useful for large-scale projects such as offshore wind farms and solar farms, where it is not practical to conduct detailed 3D FEA for hundreds or thousands of foundations during preliminary design stages.

Despite its potential, the adoption of MFDF in geotechnical engineering is still nascent, with emerging interest in areas such as predicting pipeline response to fault rupture (Dey et al. 2021) and erosion of dikes (Zhang et al. 2022). This paper investigates an MFDF design approach aimed at enhancing the accuracy of simplified design model calculations by integrating them with a small set of 3D FEA calculations, using the predictions of the static stiffness of suction caisson response in layered soils as an example. The approach involves using simplified design models to produce low-cost but potentially inaccurate calculations (referred to as 'low-fidelity data') of the caisson static stiffness. These calculations are then improved by fusing them with a small set of accurate but high-cost calculations (referred to as 'high-fidelity data') from 3D FEA models. This is achieved through the use of machine learning models that learn and exploit the cross-correlations between the low- and high-fidelity data. This paper assesses the efficacy of the MFDF approach in comparison to metamodelling, examining its dependence on training data and the limitations of the modeling approach.

Methodology

Several MFDF models have been developed over the years (Peherstorfer et al. 2018), including those based on Gaussian Process (GP) (e.g., Kennedy and O'Hagan 2000; Perdikaris et al. 2017, Feldstein et al. 2020) and deep neural networks (e.g., Meng et al. 2020, 2021; Pawar et al. 2022). The current study uses two GP-based MFDF models, which are chosen primarily for their suitability for the small training dataset in this study. The first model, a linear auto-regressive GP (LARGP), was proposed by Kennedy and O'Hagan (2000). LARGP is able to identify and model linear correlations between data of different fidelity levels. The second model, a non-linear auto-regressive GP (NARGP), was proposed by Perdikaris et al. (2017) and can model non-linear correlations between data of different fidelity levels. Thus, the difference between the LARGP and NARGP models lies in the complexity of the correlations. Both LARGP and NARGP have been successfully used for a range of scientific and engineering problems (e.g., Raissi et al. 2017; Liu et al. 2018; Liu et al. 2022; Han et al. 2022; Ferguson and Brown 2022; van de Berg et al. 2022). The following provides a summary of the theory behind LARGP and NARGP.

Gaussian Processes

A Gaussian Process (GP) is a stochastic process (i.e., a set of random variables) such that any finite number of the variables have a multivariate Gaussian distribution (Rasmussen and Williams 2006). As there is potentially an infinite number of random variables in a stochastic process, a GP can be considered as an infinite-dimensional multivariate Gaussian distribution. Another way to understand a GP is as a probability distribution over random functions, since a function can be thought of as an infinite-dimensional vector.

In GP regression, a GP prior is placed on a latent function $f(\boldsymbol{x})$. This prior is specified by a mean function $m(\boldsymbol{x})$ and covariance function (also called a kernel) $k(\boldsymbol{x}, \boldsymbol{x}')$:

$$f(\boldsymbol{x}) \sim GP\big(m(\boldsymbol{x}), k(\boldsymbol{x}, \boldsymbol{x}')\big) \tag{1}$$

where $m(\boldsymbol{x})$ represents the average of all possible functions in the distribution evaluated at input $\boldsymbol{x}$, while $k(\boldsymbol{x}, \boldsymbol{x}')$ represents the correlations between the function values at different inputs $\boldsymbol{x}$ and $\boldsymbol{x}'$. The mean function is usually assumed to be a constant mean function i.e., $m(\boldsymbol{x}) = c$ for some constant scalar c. The most commonly used covariance functions are the Squared Exponential (also called the Radial Basis) and Matérn covariance functions. For this study, the Squared Exponential covariance function is adopted and it has the following form:

$$k_{\mathrm{SE}}(\boldsymbol{x}, \boldsymbol{x}') = \sigma_f^2 \exp\left(-\frac{1}{2}\left(\frac{\boldsymbol{x}-\boldsymbol{x}'}{l}\right)^2\right) \tag{2}$$

σ_f^2 is a scaling factor that determines the variation of the function values from the mean value, while l is the lengthscale of the process (i.e., distance between inputs within which the corresponding outputs are significantly correlated). In the case of multi-dimensional inputs, the lengthscale l can be assumed to be either the same or different for each input dimension. If the lengthscale is assumed to be the same for all input dimensions, the covariance function is called 'isotropic'. Otherwise, it is called 'anisotropic'. The values of the hyperparameters, such as σ_f^2 and l in Eq. 2, are optimized using the empirical Bayes method during the training phase. This involves the maximization of the marginal log likelihood of the training data given the hyperparameters (Rasmussen and Williams 2006).

Linear Auto-Regressive Gaussian Process (LARGP)

LARGP is based on a linear autoregressive data fusion scheme that was introduced by Kennedy and O'Hagan (2000), but later improved by Le Gratiet and Garnier (2014) for enhanced computational efficiency. In this paper, it is assumed that there are s data sources $g_i(x)$ where $i \in \{1, 2, \ldots, s\}$, that can be used to estimate the output at some input $\boldsymbol{x}$. Each index i represents the fidelity of the corresponding data source, with $g_s(\boldsymbol{x})$ being the highest fidelity data source, and $g_1(\boldsymbol{x})$ being the lowest fidelity data source.

In LARGP, the prior distributions of the latent functions modeling each data source are based on Gaussian Processes. The GP prior for the fidelity model f_t for each data source is specified by a mean function $m_t(\boldsymbol{x})$ and covariance function $k_t(\boldsymbol{x}, \boldsymbol{x}')$, and is related to the GP prior for a lower-fidelity model f_{t-1} in an autoregressive manner:

$$f_t(\boldsymbol{x}) = \rho_{t-1}\, f_{t-1}(\boldsymbol{x}) + \delta_t(\boldsymbol{x}) \tag{3}$$

where ρ_{t-1} is a constant scale factor and $\delta_t(\boldsymbol{x})$ is an offset factor modeled as a GP with a mean function $m_{\delta_t}(\boldsymbol{x})$ and covariance function $k_{\delta_t}(\boldsymbol{x}, \boldsymbol{x}')$. ρ_{t-1} and $\delta_t(\boldsymbol{x})$ represent the multiplicative and additive bias between the two fidelity levels, respectively. For the current study, a constant mean function and an anisotropic Squared Exponential covariance function is used for all the mean and covariance functions in LARGP, respectively.

One advantage of this recursive inference approach is that it results in a sequence of standard GP regression, which simplifies the learning of the GP model hyperparameters and makes the training process much more computationally efficient, as it involves inversion of matrices with smaller dimensions. After the hyperparameters of LARGP have been optimized during the training phase, the posterior distributions of the predictive mean μ_t^* and variance σ^{*2}_t for each fidelity model for some input $\boldsymbol{x}_*$ can be obtained as:

$$\mu_t^*(\boldsymbol{x}_*) = \rho_{t-1}\, \mu_{t-1}^*(\boldsymbol{x}_*) + \mu_{\delta t}^*(\boldsymbol{x}_*) + \boldsymbol{k}_{*t}\boldsymbol{K}_t^{-1}\big(\boldsymbol{y}_t - \rho_{t-1}\, \mu_{t-1}^*(\boldsymbol{x}_t) - \mu_{\delta t}^*(\boldsymbol{x}_t)\big) \tag{4}$$

$$\sigma^{*2}_t(\boldsymbol{x}_*) = \rho_{t-1}^2\, \sigma^{*2}_{t-1}(\boldsymbol{x}_*) + k_{**} - \boldsymbol{k}_{*t}\boldsymbol{K}_t^{-1}\boldsymbol{k}_{*t}^T \tag{5}$$

where $\boldsymbol{x}_t$ and $\boldsymbol{y}_t$ refer to all the training inputs and outputs at fidelity level t, $\mu_{\delta t}^*$ is the posterior mean for δ_t, $k_{**} = k_t(\boldsymbol{x}_*, \boldsymbol{x}_*), \boldsymbol{k}_{*t} = \left[k_t\left(\boldsymbol{x}_*, \boldsymbol{x}_t^{(1)}\right), \ldots, k_t\left(\boldsymbol{x}_*, \boldsymbol{x}_t^{(N)}\right)\right]$ with $\boldsymbol{x}_t^{(i)}$ representing the ith input at fidelity level t, and K_t is the covariance matrix for fidelity level t with $K_{t,ij} = k_t(\boldsymbol{x}_t^{(i)}, \boldsymbol{x}_t^{(j)})$.

To clarify how LARGP works conceptually, Fig. 1 shows the fusion of a high- and low-fidelity data source that are produced synthetically for the purpose of illustration. At first glance, the low-fidelity data may appear to be a poor match for the high-fidelity data, which could lead one to dismiss it as uninformative. However, despite having limited high-fidelity training data, LARGP can accurately predict the unknown true function that generates the high-fidelity data, as shown in Fig. 1. Using this limited training data, LARGP learned that the scale factor is $\rho = 4.89$ and the average offset factor (noting that the offset factor may differ for each input) is -3.7. These values are very close to the actual values of 4.9 and -3.7, respectively (i.e., High-fidelity = 4.9*Low-fidelity – 3.7). To illustrate what would happen if the low-fidelity data were not considered, a metamodel based on a single-fidelity GP regression model (referred to in this paper as ‘GP-HF’) is trained on the high-fidelity data alone. Fig.1 demonstrates that GP-HF has good interpolation performance but poor extrapolation performance, which is caused by its poor generalization ability.

LARGP assumes a linear correlation between each fidelity model. As will be shown later, this assumption is reasonable for the stiffness estimation problem analyzed in the current study. For comparison, the current paper also implements NARGP, an extension of LARGP that allows for non-linear correlations between each fidelity model. It is of interest to see whether the NARGP model can provide more accurate predictions than LARGP, given its ability to model both linear and non-linear correlations.

Non-linear Auto-Regressive Gaussian Process (NARGP)

NARGP (Perdikaris et al. 2017) can be considered as a generalized extension of LARGP, where the GP prior for a fidelity model f_t is related to the GP posterior for the lower-fidelity model f_{t-1}^* in the following autoregressive manner:

$$f_t(\boldsymbol{x}) = h_{t-1}\left(f_{t-1}^*(\boldsymbol{x})\right) + \delta_t(\boldsymbol{x}) \tag{6}$$

where $h_{t-1}(\boldsymbol{x})$ and $\delta_t(\boldsymbol{x})$ are independent GP models, and $h_{t-1}\left(f_{t-1}^*(\boldsymbol{x})\right)$ is the composition of two GPs. To capture non-linear cross-correlations between the different fidelity models, a custom covariance function $k_t(\boldsymbol{x}, \boldsymbol{x}')$ is proposed by Perdikaris et al. (2017):

$$k_t(\boldsymbol{x}, \boldsymbol{x}') = k_{h_{t-1}}(\boldsymbol{x}, \boldsymbol{x}') \times k_{f_{t-1}}\left(f_{t-1}^*(\boldsymbol{x}), f_{t-1}^*(\boldsymbol{x}')\right) + k_{\delta_t}(\boldsymbol{x}, \boldsymbol{x}') \tag{7}$$

where $k_{h_{t-1}}$, $k_{f_{t-1}}$ and k_{δ_t} are the base covariance functions. For the current study, a constant mean function and an anisotropic Squared Exponential covariance function is used for all the mean and base covariance functions in NARGP, respectively.

The posterior distribution for $f_t(\boldsymbol{x})$ is no longer Gaussian and the non-linear mapping is no longer analytically tractable. After the hyperparameters of NARGP have been optimized during the training phase, the predictive mean μ_t^* and variance σ^{*2}_t for each fidelity model are estimated using Monte Carlo integration.

Training data

This study focuses on the estimation of the vertical, horizontal, moment, and torsional static stiffnesses of a suction caisson foundation in layered soil conditions. The soil profiles examined in the current study are three-layered, similar to those studied by Poulos (1979) for axially loaded piles in layered soil conditions, but with the additional complexity of continuously varying shear modulus within each layer (see Fig. 2). The shear modulus profile G_i in the ith layer vary with depth z according to the following equation:

$$G_i = G_i^{\text{ref}}\left(\frac{2z}{D}\right)^{\alpha} \tag{8}$$

where $i = 1, 2$ or 3 and $0 \leq \alpha \leq 1$. Table 1 provides information on the properties of these soil profiles e.g., the reference shear modulus for each layer (i.e., $G_1^{\text{ref}}, G_2^{\text{ref}}, G_3^{\text{ref}}$). The soil Poisson's ratio ν and the shear modulus depth variation parameter α are assumed to be same for all layers. Six values of $\nu = 0, 0.1, 0.2, 0.3, 0.4, 0.49$ and 3 values of $\alpha = 0, 0.5, 1$ were analyzed in the study. The results of this study apply to any caisson diameter because the employed shear modulus profiles and caisson skirt lengths are normalized by the caisson diameter. Fig. 2b shows an example shear modulus profile for Case P2 in Table 1 for $\alpha = 0.5$ and $L/D = 1$.

Several caisson length-to-diameter ratios ($L/D = 0.25, 0.5, 1, 2$) that are typical of those used for offshore wind applications are analyzed for each soil profile. A total of 432 unique combinations of caisson dimensions and soil profiles were analyzed.

While fusion of many fidelities is possible, this study considers fusion of only two fidelity levels: high-fidelity and low-fidelity. Fidelity here refers to the accuracy of the calculations given the problem assumptions, instead of how realistic the calculations are (which is dependent on the problem assumptions). The high-fidelity data corresponds to the static stiffness calculations obtained through detailed 3D FEA using Abaqus v6.13 (Dassault Systèmes 2014). The 3D FEA model used is the same as that described in Suryasentana et al. (2022) and is briefly explained below. The soil volume has three layers in accordance to Table 1. The soil is modeled as isotropic linear elastic using first-order brick elements C3D8 (or C3D8H for $\nu = 0.49$). Both the soil volume and caisson structure are assumed to be weightless, as per Suryasentana et al. (2022). The mesh domain is set to $100D$ for both width and depth (where D represents the caisson diameter), and a close-up view of half of the 3D FEA mesh near the caisson is shown in Fig. 3a. The loading reference point (LRP) is positioned at the center of the lid base (see Fig. 2). The soil-caisson interface is modeled using tie constraints to prevent contact breaking. Rigid constraints are used to model a fully rigid caisson. Displacements are prescribed at the LRP to calculate the static stiffness of the caisson response.

The low-fidelity data used in this study correspond to caisson static stiffness calculations by a simplified Winkler-based design model called OxCaisson (Suryasentana et al. 2022), as shown in Fig. 3b. The OxCaisson model was chosen for this study over other existing simplified design models (e.g., Doherty et al. 2005; Efthymiou and Gazetas 2018; Jalbi et al. 2018) as the latter are macro-element models that require the shear modulus profile to fit some idealized parametric form, which is not straightforward for the layered soil profiles examined in this study. OxCaisson, on the other hand, is a Winkler model for suction caissons that can accept arbitrary shear modulus profiles as inputs directly. OxCaisson is similar to the 'p-y' Winkler model that is commonly used to design laterally-loaded monopile foundations (e.g., API 2010; DNV 2014; Suryasentana and Lehane 2014a, 2014b, 2016), except that there are soil reactions for the full six-degrees-of-freedom (6DoF) load space. There are two types of soil reactions: distributed soil

reactions that act along the caisson skirt length, and concentrated soil reactions that act at the caisson base.

OxCaisson utilizes local soil properties to determine the soil reactions, enabling it to directly work with any shear modulus profile. However, the accuracy of its static stiffness estimations is verified only for non-layered shear modulus profiles characterized by the following equation:

$$G = G^{\mathrm{ref}} \left(\frac{2z}{D}\right)^{\alpha} \tag{9}$$

where α is a parameter that influences how the shear modulus increases with depth. Suryasentana et al. (2022) found that the soil reactions in OxCaisson depend not only on the local shear modulus values, but are also slightly influenced by the α value that most accurately represents the shear modulus profile. However, the layered shear modulus profiles examined in the current study do not align well with Eq. 9, making it challenging to assign suitable α values to these profiles. Due to this limitation, the current study defaults to using an α value of 0 when defining the soil reactions in OxCaisson to calculate the static stiffness of the caisson response. This simplifies the calculation process but leads to estimates of static stiffness that are less accurate. However, this scenario provides an opportunity to assess how well the MFDF approach can address and correct these predictive inaccuracies.

To visualise the correlations between the high- and low-fidelity data, Fig. 4 shows the relationship between the normalized stiffness calculations from the high- and low-fidelity data for all the layered soil profiles considered in this study. These normalized stiffness calculations are $\frac{K_V}{G_R D}, \frac{K_H}{G_R D}, \frac{K_Q}{G_R D^3}, \frac{K_M}{G_R D^3}$, which corresponds to the normalized vertical, horizontal, torsional and moment stiffness, respectively. G_R is the global reference shear modulus described in Table 1 and D is the caisson diameter. Fig. 4 indicates a reasonable assumption of linear correlation between the high- and low-fidelity data, albeit with some noise.

MFDF model predictions

The inputs into the MFDF and GP-HF models are $\frac{L}{D}, G_1^{\mathrm{ref}}, G_2^{\mathrm{ref}}, G_3^{\mathrm{ref}}, \nu, \alpha$ and the outputs are the static stiffnesses of the suction caisson foundations. During the training process, the MFDF

models receive both high-fidelity and corresponding low-fidelity data to learn the correlations between them. Once trained, the MFDF models can predict the static stiffness of a suction caisson foundation for a given input by taking the low-fidelity prediction for that input and applying the learnt correlations to enhance its accuracy. The training and operational phases of the MFDF models are summarized in Fig. 5.

Evaluation focus

This study will evaluate three different aspects of the MFDF models (i.e., LARGP and NARGP). Firstly, the sensitivity of the predictive performance to the number of high-fidelity training data is examined. To assess this, the full high-fidelity dataset is first split into training and test datasets in a 60:40 ratio, with the training dataset referred to as TD60. Three smaller training datasets are then created by taking random subsets of TD60, which are equivalent to 30% (TD30), 15% (TD15), and 7% (TD7) of the full high-fidelity dataset, respectively. That is equivalent to about 259, 129, 64 and 32 data points for each stiffness prediction task for T60, T30, T15 and TD7, respectively. For every dataset, there is generally a balanced distribution of each of the six input parameters, e.g., the L/D parameter is evenly distributed between its possible values of 0.25, 0.5, 1 and 2. The predictive performance of the MFDF models trained on each of these training datasets will be compared. This provides insights into the minimum quantity of data required for reasonably accurate predictions, and the added value of acquiring more high-fidelity data.

Secondly, the sensitivity of the predictive performance to the composition of the training data will be examined. To this end, 20 random samplings of the four training datasets (TD60, TD30, TD15, TD7) and the test dataset are generated. The mean and variance of the predictive performance of the MFDF models trained on these training datasets will be examined to see if the accuracy of the MFDF models varied significantly as the composition of the training and test data changed.

Finally, the improvement in the predictive performance facilitated by MFDF will be examined by comparison to a metamodel based on a single-fidelity GP regression model (referred to in this paper as ‘GP-HF’), which is trained on the high-fidelity data alone. GP-HF will also use a constant mean function and an anisotropic Squared Exponential covariance function.

Results

To demonstrate how MFDF would work conceptually for the static stiffness problem, LARGP is applied to a simplified problem of predicting the vertical stiffness of a suction caisson in a specific layered soil configuration (Case P2 in Table 1 for $\alpha = 0$). The input into LARGP is L/D, which makes this a simple one-dimensional predictive problem. There are four high-fidelity data points, with half used for training and the other half for testing. Fig. 6a compares the vertical stiffness predicted by LARGP with that predicted by GP-HF. Firstly, it can be observed that the LARGP predictions match the test data very well, while the GP-HF predictions were less satisfactory. Secondly, GP-HF performs poorly with its (extrapolation) predictions for $L/D = 2$ compared to its (interpolation) predictions for $L/D = 0.5$, whereas LARGP predictions perform well in both cases. Therefore, the inclusion of low-fidelity data, which are quantitatively imprecise but correct trend-wise, helps to improve the extrapolation performance for this particular example. Note that the accuracy of the extrapolation performance of LARGP may be lower for much larger L/D ratios as the trend may change as L/D increases.

Fig. 7 compares the static stiffnesses predicted by the MFDF and GP-HF models (all trained on the TD60 training dataset) with the actual values from the high-fidelity test dataset. It can be observed that both LARGP and NARGP have excellent agreement with the test dataset for all stiffnesses. The GP-HF model's predictions are in good agreement with the test dataset. However, it is less accurate in predicting the moment stiffness. (see Fig. 7d).

To evaluate the impact of the amount of training data on model performance, Figs. 8 to 10 evaluate the predictions of the models using the same test dataset, but with the models trained on decreasing subsets of the original training data (from 30% to 7% of the full high-fidelity dataset). As the amount of training data decreases, LARGP maintains excellent agreement with the test dataset and only displays a noticeable loss of accuracy when the amount of training data decreases to 7%, as shown in Fig. 10. In contrast, both NARGP and GP-HF begin to lose accuracy when the amount of training data falls below 30% of the full dataset, as shown in Figs. 9 and 10.

To better quantify the accuracy of the models, Table 2 provides the root-mean-square (RMS) errors between the model predictions of all the static stiffnesses and the actual values from the test dataset for the different training datasets. The RMS errors are calculated as follows:

$$RMS = \sqrt{\frac{\sum_{i=1}^{n}(y_i - \hat{y}_i)^2}{n}} \quad (10)$$

where n is number of data, y_i are the true FEA values from the test dataset and $\hat{y}_i$ are the predicted FEA values by the models. The table shows that the LARGP model has the highest level of accuracy, followed by NARGP and GP-HF. The RMS errors for the low-fidelity data are also provided to give an indication of its relative inaccuracy compared to the high-fidelity data. Note that the RMS errors for the low-fidelity data is independent of the training dataset sizes as they are generated by OxCaisson, which does not require training. Fig. 11a further clarifies the relationship between the RMS errors and the size of the training data. It is clear that the RMS error decreases as the number of training data increases. Moreover, the MFDF models are more accurate than OxCaisson for all training dataset sizes, while GP-HF is more accurate than OxCaisson for all training dataset sizes except when it is 7% of the full dataset.

To assess how the composition of the training data affects the predictive accuracy of the models, Table 3 shows the average and standard deviation of the RMS errors calculated for the models, given 20 random samplings of the training and test datasets. Additionally, Fig. 12 shows the coefficient of variation (COV) values of the RMS errors listed in Table 3. The results suggest that there is no clear relationship between the COV of the RMS errors and the size of the training dataset. The results also show that NARGP has the highest sensitivity to the training data composition as it generally exhibits the highest COV across most of the training data sizes.

Discussion

Fig. 11a shows that LARGP is the least sensitive to the number of training data, as its predictions remain robust and lose accuracy very gradually as the number of training data decreases. This underscores the benefits of data fusion. Even if the low-fidelity data is quantitatively inaccurate, the underlying trend predicted by the low-fidelity data can still be useful in the absence of high-fidelity training data. This is not surprising, given that the low-

fidelity data are generated by a physics-based model, albeit a highly simplified one, and the MFDF predictions benefit from the physical laws and principles embedded within the simplified design model calculations.

The results suggest that MFDF is highly suitable for large-scale foundation design projects, such as offshore wind farms, where obtaining high-fidelity calculations for all foundations can be computationally expensive. By using MFDF, it is possible to achieve a 3D FEA comparable level of accuracy for the entire wind farm site at a fraction of the computational costs, since 3D FEA calculations are only required for a fraction of the total number of foundations. Fig. 10 shows that LARGP can achieve reasonable approximations of the 3D FEA results with only 7% of the total dataset, or about 32 simulations in this study. Table 3 also demonstrates that the accuracy of LARGP is not too sensitive to the training dataset composition, thus suggesting that the careful selection of soil profiles for inclusion into the training dataset may not be a critical factor. One question that emerges is how to determine that 32 FEA simulations is sufficient for LARGP to generate reasonably accurate predictions, without the benefit of hindsight comparisons against the full dataset. A potential approach is to start with a small FEA training set (e.g., ten simulations). Then, randomly select 70% of it to train the LARGP model and use the other 30% to evaluate the RMS error of the LARGP predictions. Thereafter, expand the FEA training set and repeat the evaluation process, until the rate of decrease in RMS error stabilizes. Figure 11b illustrates the RMS error of the LARGP predictions as the number of FEA simulations increases. It can be observed that the rate of RMS error reduction stabilizes around 35 simulations, which aligns with the hindsight analysis of 32 simulations in Figure 10. For this study, accumulation of additional FEA data could cease after approximately 35 simulations.

To benefit from MFDF, selecting the appropriate MFDF model that fits the specific problem is crucial. Table 3 indicates that in data-limited situations like TD7, NARGP has lower mean accuracy than OxCaisson. Therefore, using more advanced MFDF models does not necessarily translate to better results. Instead, ensuring that the model's assumptions are compatible with the problem is of greater importance, leading to better outcomes. Some plausible reasons for LARGP’s outperformance over NARGP are discussed below.

Figure 12 reveals that LARGP is significantly more stable and less sensitive to random samplings of training data compared to NARGP. NARGP shows a high degree of variance in its predictive accuracy, depending on the composition of the training data. One possible explanation for this is that NARGP is a more complex MFDF model than LARGP, and there are numerous locally optimal hyperparameters that the training process could converge onto, leading to widely varying predictions. Table 3 indicates that LARGP is more accurate than NARGP, which may seem surprising as NARGP is a more flexible model, capable of modeling both linear and non-linear correlations between the high- and low-fidelity data. One possible reason for this is that the high- and low-fidelity data exhibit approximately linear correlations (as shown in Fig. 4), which allows for more effective hyperparameter training for the simpler LARGP model architecture. In addition to robustness and accuracy, LARGP offers other advantages over NARGP for the stiffness prediction problem. LARGP is more computationally efficient than NARGP. Using a computer with an Intel i7 2.8 GHz processor (eight central processing units) and 8 GB of RAM, LARGP took a total of 15 seconds to be trained on TD60 and make the predictions shown in Fig. 7, while NARGP took 2 minutes. This is due to the simpler model architecture of LARGP, which allows for faster training of hyperparameters. LARGP is also more interpretable than NARGP. For example, Fig. 13 shows the trained scale factor ρ and offset factors δ of LARGP to predict the normalized vertical stiffness of the caisson in Fig. 7a. The LARGP predictions can be explained as being the low-fidelity data being scaled up by 1.93 and then offset by a range of values from -30 to 15 (depending on the inputs). It is important to note that, while LARGP is performant in the current study, it may not be the optimal choice for all engineering problems. If the high- and low-fidelity data exhibits highly non-linear correlations, NARGP is likely to perform better than LARGP.

While the current study provides valuable insights, there are some limitations. The current study only considered three-layered soil profiles. However, real-world soil profiles may have more complex structures with different numbers and thicknesses of layers. A plausible solution is to adopt a soil profile structure with more layers, which would allow for improved piecewise approximation of arbitrary shear modulus profiles, as done by Minga and Burd (2019). The current study also did not consider structural factors such as caisson skirt and lid flexibility,

which have an influence on the static stiffness response and should be considered for the deployment of the proposed approach in design (Doherty et al. 2005; Skau et al. 2019). The consideration of both the soil layering structure and the structural factors would increase the number of input parameters and the performance of the MFDF approach for such high-dimensional problems with many inputs requires further investigation. Moreover, this study used the OxCaisson model predictions as the low-fidelity data. It is uncertain how the MFDF approach would perform if the low-fidelity data is determined using other simplified design models (e.g., Doherty et al. 2005; Efthymiou and Gazetas 2018; Skau et al. 2019; Jalbi et al. 2018, Suryasentana and Mayne 2022, Suryasentana et al. 2023a). Finally, this study applied the MFDF approach to estimate the static stiffness of caissons. The applicability of the MFDF approach to other design aspects of caisson foundations, such as their ultimate capacities or cyclic behaviour, warrants further investigation. For example, low-fidelity data for foundation capacities may be generated using failure envelope models (e.g., Gourvenec and Barnett 2011; Larsen et al. 2013; Hung and Kim 2014; Vulpe 2015; Suryasentana et al. 2020a, 2020b, 2021) and the high-fidelity data may be generated using 3D FEA (e.g., Achmus et al. 2013; Thieken et al. 2014). However, the implementation methodology to adapt the MFDF approach for the other design aspects needs investigation. Future work should focus on addressing these limitations.

The proposed MFDF approach is intended to complement existing simplified design models rather than replace them. Simplified design models have the advantage of being ‘rule-based’ (requiring no training process) and easy to interpret. However, when a limited number of high-fidelity (e.g., 3D FEA) data are available, the MFDF approach offers a promising solution to combine information from multiple physics-based models of varying fidelity to provide more accurate predictions than the simplified design model. The MFDF approach can be applied across multiple projects where the 3D FEA training data accumulates. This creates a self-improving framework where the MFDF approach improves its accuracy over time, as it learns from more 3D FEA data that cover a wider range of soil conditions and caisson dimensions.

Conclusion

This paper presents a multi-fidelity data fusion (MFDF) approach for estimating the static stiffness of suction caisson foundations in layered soil conditions. The proposed approach combines low-fidelity calculations from simplified design models with high-fidelity calculations from 3D FEA models. This enables greater training data efficiency compared to single-fidelity models, making it more practical for large-scale foundation design optimization. The study evaluates two GP-based MFDF models, LARGP and NARGP, and compares their predictive accuracy to that of a single-fidelity model. The results demonstrate that LARGP outperforms NARGP in terms of accuracy, computational efficiency, prediction robustness, and sensitivity to training data composition. Furthermore, LARGP achieves better accuracy than the single-fidelity model and simplified design model, even when trained with limited data. The study highlights the importance of selecting an appropriate MFDF model that fits the problem being considered, in order to fully benefit from MFDF.

Data availability statement

Some or all data, models, or code that support the findings of this study are available from the corresponding author upon reasonable request.

Acknowledgements

The second author is funded by the Royal Academy of Engineering under the Research Fellowship scheme.

Competing interests statement

Competing interests: The authors declare there are no competing interests.

Funding statement

Funding: The authors declare no specific funding for this work.

List of notations

z	depth below ground level
D	caisson diameter
L	caisson skirt length
G	shear modulus of soil
ν	Poisson's ratio of soil
α	parameter governing the change of the soil shear modulus profile with depth
G_{R}	global reference shear modulus value
K_V	vertical stiffness of the soil-foundation interaction
K_H	lateral stiffness of the soil-foundation interaction
K_M	rotational stiffness of the soil-foundation interaction
K_Q	torsional stiffness of the soil-foundation interaction
p_{atm}	atmospheric pressure
ρ	scale factor for LARGP
δ	offset factor for LARGP

References

Achmus, M., Akdag, C. T., and Thieken, K. (2013). Load-bearing behavior of suction bucket foundations in sand. *Applied Ocean Research*, *43*, 157-165.

Andersen, K.,H., Jostad, H. P. and Dyvik, R. (2008). Penetration resistance of offshore skirted foundations and anchors in dense sand. J. Geotech. Geoenviron. Engng, ASCE 134, No. 1, 106–116.

Antoniou, M., Kourkoulis, R., Gelagoti, F., and Anastasopoulos, I. (2022). Simplified method for performance-based seismic design of suction caissons supporting jacket offshore wind turbines. Soil Dynamics and Earthquake Engineering, 155, 107169.

API (2010). RP 2A-WSD - Recommended Practice for Planning, Designing and Constructing Fixed Offshore Platforms. Washington: American Petroleum Institute

Bagheri, P., Son, S. W., and Kim, J. M. (2017). Investigation of the load-bearing capacity of suction caissons used for offshore wind turbines. Applied Ocean Research, 67, 148-161.

Barari, A., Ibsen, L. B., Taghavi Ghalesari, A., and Larsen, K. A. (2017). Embedment effects on vertical bearing capacity of offshore bucket foundations on cohesionless soil. International Journal of Geomechanics, 17(4), 04016110.

Burd, H. J., Abadie, C. N., Byrne, B. W., Houlsby, G. T., Martin, C. M., McAdam, R. A., Jardine, R.J., Pedro, A.M., Potts, D.M., Taborda, D.M., Zdravković, L., and Andrade, M.P. (2020). Application of the PISA Design Model to Monopiles Embedded in Layered Soils. Géotechnique 70(11): 1-55. https://doi.org/10.1680/jgeot.20.PISA.009

Byrne, B.W. and Houlsby, G. T. (2003). Foundations for offshore wind turbines. Philosophical transactions. Series A, Mathematical, physical, and engineering sciences 361(1813), 2909–30.

Byrne, B.W., Aghakouchak, A., Buckley, R.M., Burd, H.J., Gengenbach, J., Houlsby, G.T., McAdam, R.A., Martin, C.M., Schranz, F., Sheil, B.B. and Suryasentana, S.K. (2020). PICASO: Cyclic lateral loading of offshore wind turbine monopiles. In Frontiers in Offshore Geotechnics IV: Proceedings of the 4th International Symposium on Frontiers in Offshore Geotechnics (ISFOG 2021).

Dassault Systemes (2014). Abaqus user manual. Simula Corp., Providence, RI.

Dey, S., Chakraborty, S., and Tesfamariam, S. (2021). Multi-fidelity approach for uncertainty quantification of buried pipeline response undergoing fault rupture displacements in sand. *Computers and Geotechnics*, *136*, 104197.

Díaz, H., and Soares, C. G. (2020). Review of the current status, technology and future trends of offshore wind farms. Ocean Engineering, 209, 107381.

DNV (2014). OS-J101 - Design of Offshore Wind Turbine Structures. Oslo: Det Norske Veritas.

Doherty, J. P., Houlsby, G. T., and Deeks, A. J. (2005), Stiffness of flexible caisson foundations embedded in nonhomogeneous elastic soil, Journal of Geotechnical and Geoenvironmental Engineering 131 (12), 1498–1508.

Efthymiou, G. and Gazetas, G. (2018), Elastic Stiffnesses of a Rigid Suction Caisson and Its Cylindrical Sidewall Shell, Journal of Geotechnical and Geoenvironmental Engineering 145 (2), 06018014.

Esfeh, P. K., and Kaynia, A. M. (2020). Earthquake response of monopiles and caissons for Offshore Wind Turbines founded in liquefiable soil. *Soil Dynamics and Earthquake Engineering*, *136*, 106213.

Feldstein, A., Lazzara, D., Princen, N., and Willcox, K. (2020). Multifidelity data fusion: Application to blended-wing-body multidisciplinary analysis under uncertainty. AIAA Journal, 58(2), 889-906.

Ferguson, A. L., and Brown, K. A. (2022). Data-driven design and autonomous experimentation in soft and biological materials engineering. Annual Review of Chemical and Biomolecular Engineering, 13, 25-44.

Foglia, A., Gottardi, G., Govoni, L., and Ibsen, L. B. (2015). Modelling the drained response of bucket foundations for offshore wind turbines under general monotonic and cyclic loading. Applied Ocean Research, 52, 80-91.

Gelagoti, F., Georgiou, I., Kourkoulis, R., and Gazetas, G. (2018). Nonlinear lateral stiffness and bearing capacity of suction caissons for offshore wind-turbines. Ocean Engineering, 170, 445-465.

Gourvenec, S. and Barnett, S. (2011). Undrained failure envelope for skirted foundations under general loading. Géotechnique, 61(3), 263–270.

Han, T., Ahmed, K. S., Gosain, A. K., Tepole, A. B., and Lee, T. (2022). Multi-Fidelity Gaussian Process Surrogate Modeling of Pediatric Tissue Expansion. Journal of Biomechanical Engineering, 144(12), 121005.

He, B., Jiang, J., Cheng, J., Zheng, J., and Wang, D. (2021). The capacities of tripod bucket foundation under uniaxial and combined loading. Ocean Engineering, 220, 108400.

Houlsby, G. T., and Byrne, B. W. (2005a). Design procedures for installation of suction caissons in sand. Proceedings of the Institution of Civil Engineers-Geotechnical Engineering, 158(3), 135-144.

Houlsby, G. T., and Byrne, B. W. (2005b). Design procedures for installation of suction caissons in clay and other materials. Proceedings of the Institution of Civil Engineers-Geotechnical Engineering, 158(2), 75-82.

Hung, L. C. and Kim, S. (2014). Evaluation of undrained bearing capacities of Bucket Foundations Under Combined Loads. Marine Georesources and Geotechnology, 32(1), 76–92.

Jalbi, S., Shadlou, M., and Bhattacharya, S. (2018). Impedance functions for rigid skirted caissons supporting offshore wind turbines. Ocean Engineering, 150, 21-35.

Kang, F., Han, S., Salgado, R., and Li, J. (2015). System probabilistic stability analysis of soil slopes using Gaussian process regression with Latin hypercube sampling. Computers and Geotechnics, 63, 13-25.

Kennedy, M. C., and O'Hagan, A. (2000). Predicting the output from a complex computer code when fast approximations are available. *Biometrika*, *87*(1), 1-13.

Kourkoulis, R. S., Lekkakis, P. C., Gelagoti, F. M., and Kaynia, A. M. (2014). Suction caisson foundations for offshore wind turbines subjected to wave and earthquake loading: effect of soil–foundation interface. Géotechnique, 64(3), 171-185.

Larsen, K. A., Ibsen, L. B., and Barari, A. (2013). Modified expression for the failure criterion of bucket foundations subjected to combined loading. Canadian Geotechnical Journal, 50(12), 1250-1259.

Latini, C., and Zania, V. (2017). Dynamic lateral response of suction caissons. Soil Dynamics and Earthquake Engineering, 100, 59-71.

Le Gratiet, L., and Garnier, J. (2014). Recursive co-kriging model for design of computer experiments with multiple levels of fidelity. *International Journal for Uncertainty Quantification*, *4*(5).

Liu, H., Ong, Y. S., and Cai, J. (2018). A survey of adaptive sampling for global metamodeling in support of simulation-based complex engineering design. Structural and Multidisciplinary Optimization, 57, 393-416.

Liu, M., Yang, M., and Wang, H. (2014). Bearing behavior of wide-shallow bucket foundation for offshore wind turbines in drained silty sand. Ocean Engineering, 82, 169-179.

Liu, T., Zhang, Y., and Meng, Q. (2023). Numerical investigation and design of suction caisson for on-bottom pipelines under combined VHMT loading in normal consolidated clay. Ocean Engineering, 274, 113997.

Liu, X., Zhao, W., and Wan, D. (2022). Multi-fidelity Co-Kriging surrogate model for ship hull form optimization. Ocean Engineering, 243, 110239.

Meng, X. and Karniadakis, G. E. (2020). A composite neural network that learns from multi-fidelity data: Application to function approximation and inverse PDE problems. Journal of Computational Physics, 401, 109020.

Meng, X., Babaee, H., and Karniadakis, G. E. (2021). Multi-fidelity Bayesian neural networks: Algorithms and applications. *Journal of Computational Physics*, *438*, 110361.

Mentani, A., Govoni, L., Bourrier, F., and Zabatta, R. (2023). Metamodelling of the load-displacement response of offshore piles in sand. Computers and Geotechnics, 159, 105490.

Minisci, E., Vasile, M., and Liqiang, H. (2011). Robust multi-fidelity design of a micro re-entry unmanned space vehicle. Proceedings of the Institution of Mechanical Engineers, Part G: Journal of Aerospace Engineering, 225(11), 1195-1209.

Minga, E. and Burd, H.J. (2019). Validation of PLAXIS MoDeTo based on the Cowden Till PISA Field Tests. Oxford University Report. Oxford, UK.

Nielsen, S. D. (2019). Finite element modeling of the tensile capacity of suction caissons in cohesionless soil. Applied Ocean Research, 90, 101866.

Pawar, S., San, O., Vedula, P., Rasheed, A., and Kvamsdal, T. (2022). Multi-fidelity information fusion with concatenated neural networks. *Scientific Reports*, *12*(1), 5900.

Peherstorfer, B., Willcox, K., and Gunzburger, M. (2018). Survey of multifidelity methods in uncertainty propagation, inference, and optimization. *Siam Review*, *60*(3), 550-591.

Perdikaris, P., Raissi, M., Damianou, A., Lawrence, N. D., and Karniadakis, G. E. (2017). Nonlinear information fusion algorithms for data-efficient multi-fidelity modelling. *Proceedings of the Royal Society A: Mathematical, Physical and Engineering Sciences*, *473*(2198), 20160751.

Poulos, H. G. (1979). Settlement of single piles in non homogeneous soil. Journal of Geotechnical Engineering Division ASCE, 105(5), 627–641.

Raissi, M., Perdikaris, P., and Karniadakis, G. E. (2017). Machine learning of linear differential equations using Gaussian processes. Journal of Computational Physics, 348, 683-693.

Rasmussen, C. E., and Williams, C. K. (2006). Gaussian processes for machine learning (Vol. 1, p. 159). Cambridge, MA: MIT press.

Samui, P., Das, S., and Kim, D. (2011). Uplift capacity of suction caisson in clay using multivariate adaptive regression spline. Ocean Engineering, 38(17-18), 2123-2127.

Senders, M., and Randolph, M. F. (2009). CPT-based method for the installation of suction caissons in sand. Journal of geotechnical and geoenvironmental engineering, 135(1), 14-25.

Shen, Q., Vahdatikhaki, F., Voordijk, H., van der Gucht, J., and van der Meer, L. (2022). Metamodel-based generative design of wind turbine foundations. Automation in construction, 138, 104233.

Skau K. S., Grimstad G., Page A. M., Eiksund G. R. and Jostad H. P. (2018). A macro-element for integrated time domain analyses representing bucket foundations for offshore wind turbines. Marine Structures, 59, 158–78.

Skau K. S., Jostad H. P., Eiksund G., Sturm H. P. (2019) Modelling of soil-structure-interaction for flexible caissons for offshore wind turbines. Ocean Engineering, 171, 273–85.

Soubra, A. H., Al-Bittar, T., Thajeel, J., and Ahmed, A. (2019). Probabilistic analysis of strip footings resting on spatially varying soils using kriging metamodeling and importance sampling. Computers and Geotechnics, 114, 103107.

Sturm, H. (2017). Design aspects of suction caissons for offshore wind turbine foundations. In Unearth the Future, Connect beyond. Proceedings of the 19th International Conference on Soil Mechanics and Geotechnical Engineering.

Suryasentana, S. K., and Lehane, B. M. (2014a). Numerical derivation of CPT-based p–y curves for piles in sand. Géotechnique, 64(3), 186-194.

Suryasentana, S. K., and Lehane, B. M. (2014b). Verification of numerically derived CPT based py curves for piles in sand. In Proceedings of 3rd International Symposium on Cone Penetration Testing (pp. 3-29). Las Vegas, Nevada USA.

Suryasentana, S. K., & Lehane, B. M. (2016). Updated CPT-based p–y formulation for laterally loaded piles in cohesionless soil under static loading. Géotechnique, 66(6), 445-453.

Suryasentana, S. K., Byrne, B. W., Burd, H. J., and Shonberg, A. (2017). Simplified model for the stiffness of suction caisson foundations under 6DoF loading. In Proceedings of SUT OSIG 8th International Conference, London, UK.

Suryasentana, S. K., Byrne, B. W., Burd, H. J., and Shonberg, A. (2018). An elastoplastic 1D Winkler model for suction caisson foundations under combined loading. Numerical Methods in Geotechnical Engineering IX, 973-980. CRC Press.

Suryasentana, S., Byrne, B., and Burd, H. (2019). Automated optimization of suction caisson foundations using a computationally efficient elastoplastic Winkler model. Coastal Structures 2019, 932-941.

Suryasentana, S. K., Burd, H. J., Byrne, B. W., and Shonberg, A. (2020a). A systematic framework for formulating convex failure envelopes in multiple loading dimensions. Géotechnique, 70(4), 343-353.

Suryasentana, S. K., Dunne, H. P., Martin, C. M., Burd, H. J., Byrne, B. W., and Shonberg, A. (2020b). Assessment of numerical procedures for determining shallow foundation failure envelopes. Géotechnique, 70(1), 60-70.

Suryasentana, S. K., Burd, H. J., Byrne, B. W., and Shonberg, A. (2021). Automated procedure to derive convex failure envelope formulations for circular surface foundations under six degrees of freedom loading. Computers and Geotechnics, 137, 104174.

Suryasentana, S. K., Burd, H. J., Byrne, B. W., and Shonberg, A. (2022). A Winkler model for suction caisson foundations in homogeneous and non-homogeneous linear elastic soil. Géotechnique, 7and2(5), 407-423.

Suryasentana, S. K., and Mayne, P. W. (2022). Simplified method for the lateral, rotational, and torsional static stiffness of circular footings on a nonhomogeneous elastic half-space based on a work-equivalent framework. Journal of Geotechnical and Geoenvironmental Engineering, 148(2), 04021182.

Suryasentana, S. K., Burd, H. J., Byrne, B. W., and Shonberg, A. (2023a). Modulus weighting method for stiffness estimations of suction caissons in layered soils. Géotechnique Letters, 13(2), 1-8.

Suryasentana, S. K., Burd, H. J., Byrne, B. W., & Shonberg, A. (2023b). Small-strain, non-linear elastic Winkler model for uniaxial loading of suction caisson foundations. Géotechnique Letters, 1-26.

Thieken, K., Achmus, M., and Schröder, C. (2014). On the behavior of suction buckets in sand under tensile loads. Computers and Geotechnics, 60, 88-100.

Ukritchon, B., and Keawsawasvong, S. (2016). Undrained pullout capacity of cylindrical suction caissons by finite element limit analysis. Computers and Geotechnics, 80, 301-311.

van de Berg, D., Savage, T., Petsagkourakis, P., Zhang, D., Shah, N., and del Rio-Chanona, E. A. (2022). Data-driven optimization for process systems engineering applications. Chemical Engineering Science, 248, 117135.

Vulpe, C. (2015). Design method for the undrained capacity of skirted circular foundations under combined loading: effect of deformable soil plug. Géotechnique, 65(8), 669-683.

Wang, H., and Cheng, X. (2016). Undrained bearing capacity of suction caissons for offshore wind turbine foundations by numerical limit analysis. Marine Georesources and Geotechnology, 34(3), 252-264.

Wang, Q., and Owens, P. (2022). Reliability-based design optimisation of geotechnical systems using a decoupled approach based on adaptive metamodels. Georisk: Assessment and Management of Risk for Engineered Systems and Geohazards, 16(3), 470-488.

Wang, X., Yu, L., Yang, Q., and Tang, X. (2022). The drained tension capacity of suction buckets in sand under vertical uplift loading. Ocean Engineering, 266, 113169.

Wu, Y., Yang, Q., Li, D., and Zhang, Y. (2022). Limit equilibrium solutions to anti-overturning bearing capacity of suction caissons in uniform and linearly increasing strength clays. *Canadian Geotechnical Journal*, *59*(2), 304-313.

Yang, X., Zeng, X., and Wang, X. (2018). Lateral-moment loading capacity and bearing behavior of suction bucket foundations for offshore wind turbines in sand. *International Journal of Geomechanics*, *18*(11), 04018152.

Yin, Z. Y., Teng, J. C., Li, Z., and Zheng, Y. Y. (2020). Modelling of suction bucket foundation in clay: From finite element analyses to macro-elements. Ocean Engineering, 210, 107577.

Yin, X., Wang, H., Pisanò, F., Gavin, K., Askarinejad, A., and Zhou, H. (2023). Deep learning-based design model for suction caissons on clay. Ocean Engineering, 286, 115542.

Zhang, P., Yin, Z. Y., Jin, Y. F., Yang, J., and Sheil, B. (2022). Physics-informed multifidelity residual neural networks for hydromechanical modeling of granular soils and foundation considering internal erosion. *Journal of Engineering Mechanics*, *148*(4), 04022015.

Zhu, F. Y., O'Loughlin, C. D., Bienen, B., Cassidy, M. J., and Morgan, N. (2018). The response of suction caissons to long-term lateral cyclic loading in single-layer and layered seabeds. Géotechnique, 68(8), 729-741.

Zhu, F. Y., Bienen, B., O'Loughlin, C., Cassidy, M. J., and Morgan, N. (2019). Suction caisson foundations for offshore wind energy: Cyclic response in sand and sand over clay. Géotechnique, 69(10), 924-931.

Table 1 Shear modulus profiles for three-layered soil profiles analyzed in the numerical study (see Fig. 2a), where the shear modulus profile in each layer is described by Eq. 8. $G_R = 1000p_{\mathrm{atm}}$ is the global reference shear modulus value and L is the caisson skirt length.

	Reference shear modulus for each layer		
Name	G_1^{ref}/G_R $(z/D < 0.3L/D)$	G_2^{ref}/G_R $(0.3L/D \leq z/D < 0.7L/D)$	G_3^{ref}/G_R $(z/D \geq 0.7L/D)$
P1	1	2	4
P2	1	4	2
P3	2	1	4
P4	2	4	1
P5	4	2	1
P6	4	1	2

Table 2 Calculations of root-mean-square (RMS) errors of the model predictions for different training data sizes (i.e., TD60, TD30, TD15, TD7), but for the same test dataset.

Model	**RMS Error (TD60)**	**RMS Error (TD30)**	**RMS Error (TD15)**	**RMS Error (TD7)**
LARGP	0.33	0.80	2.75	4.00
NARGP	1.76	4.86	8.13	12.11
GP-HF	3.77	5.96	9.67	14.92
OxCaisson	13.89	13.89	13.89	13.89

Table 3 Calculations of the average RMS errors (±one standard deviation) of the model predictions for different training data sizes (i.e., TD60, TD30, TD15, TD7), given 20 random samplings of the training and test datasets.

Model	**Average RMS Error (TD60)**	**Average RMS Error (TD30)**	**Average RMS Error (TD15)**	**Average RMS Error (TD7)**
LARGP	0.23 (±0.06)	0.97 (±0.46)	3.52 (±1.72)	5.81 (±1.88)
NARGP	0.83 (±0.76)	5.68 (±3.94)	9.45 (±5.76)	16.59 (±8.54)
GP-HF	3.19 (±1.37)	6.11 (±1.58)	10.20 (±4.14)	17.75 (±7.68)
OxCaisson	12.97 (±1.05)	12.97 (±1.05)	12.97 (±1.05)	12.97 (±1.05)

Figures

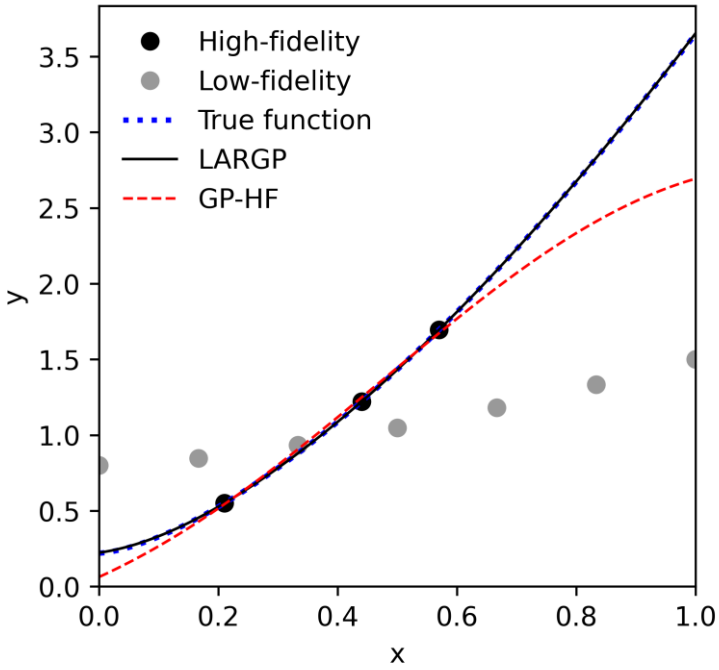

Figure 1 Illustrative example showing the predictive capabilities of LARGP, even with limited high-fidelity training data. GP-HF is the machine learning model trained on high-fidelity data alone.

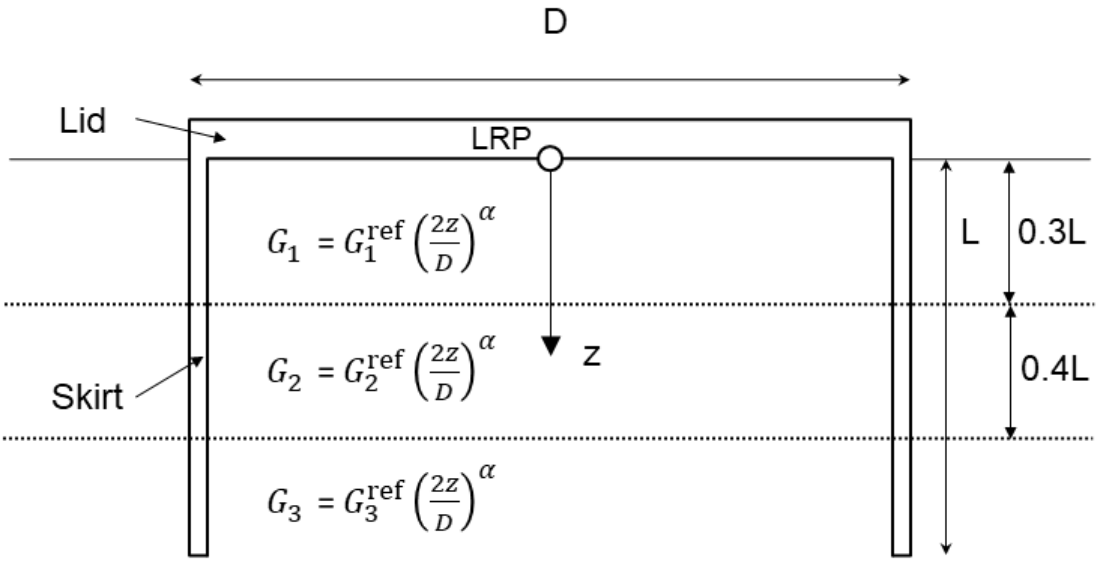

(a)

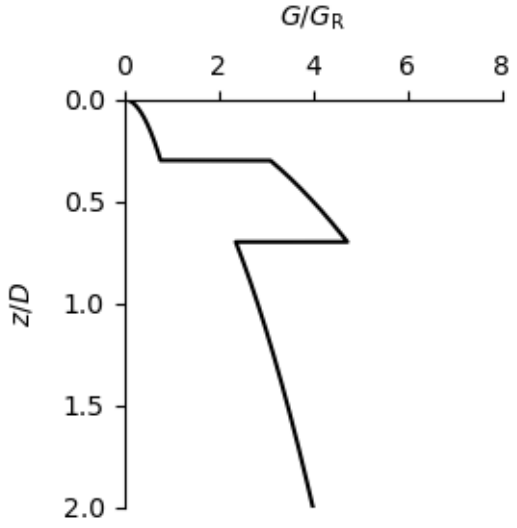

(b)

Figure 2 (a) Schematic diagram of a suction caisson foundation and the three-layered soil profiles investigated in this paper. The loading reference point (LRP) is at the center of the caisson lid base. (b) Exemplar shear modulus profile for Case P2 of Table 1 for $\alpha = 0.5$ and $L/D = 1$.

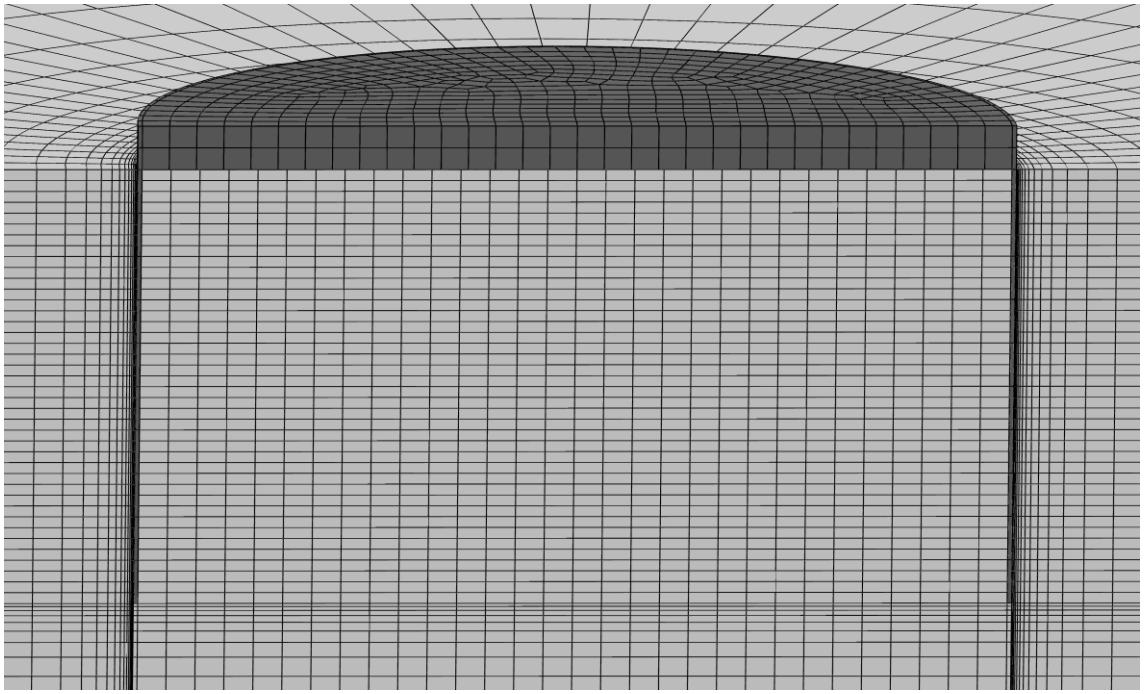

(a)

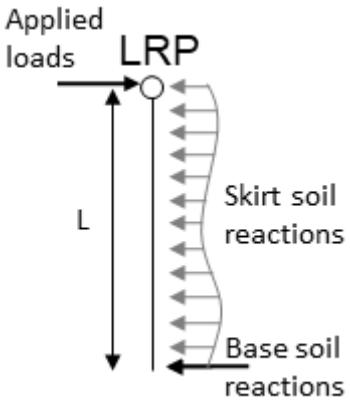

(b)

Figure 3 (a) Close-up view of the half of the 3D FEA mesh around the suction caisson. (b) Schematic diagram of the one-dimensional Winkler model of the suction caisson foundation as modeled in OxCaisson.

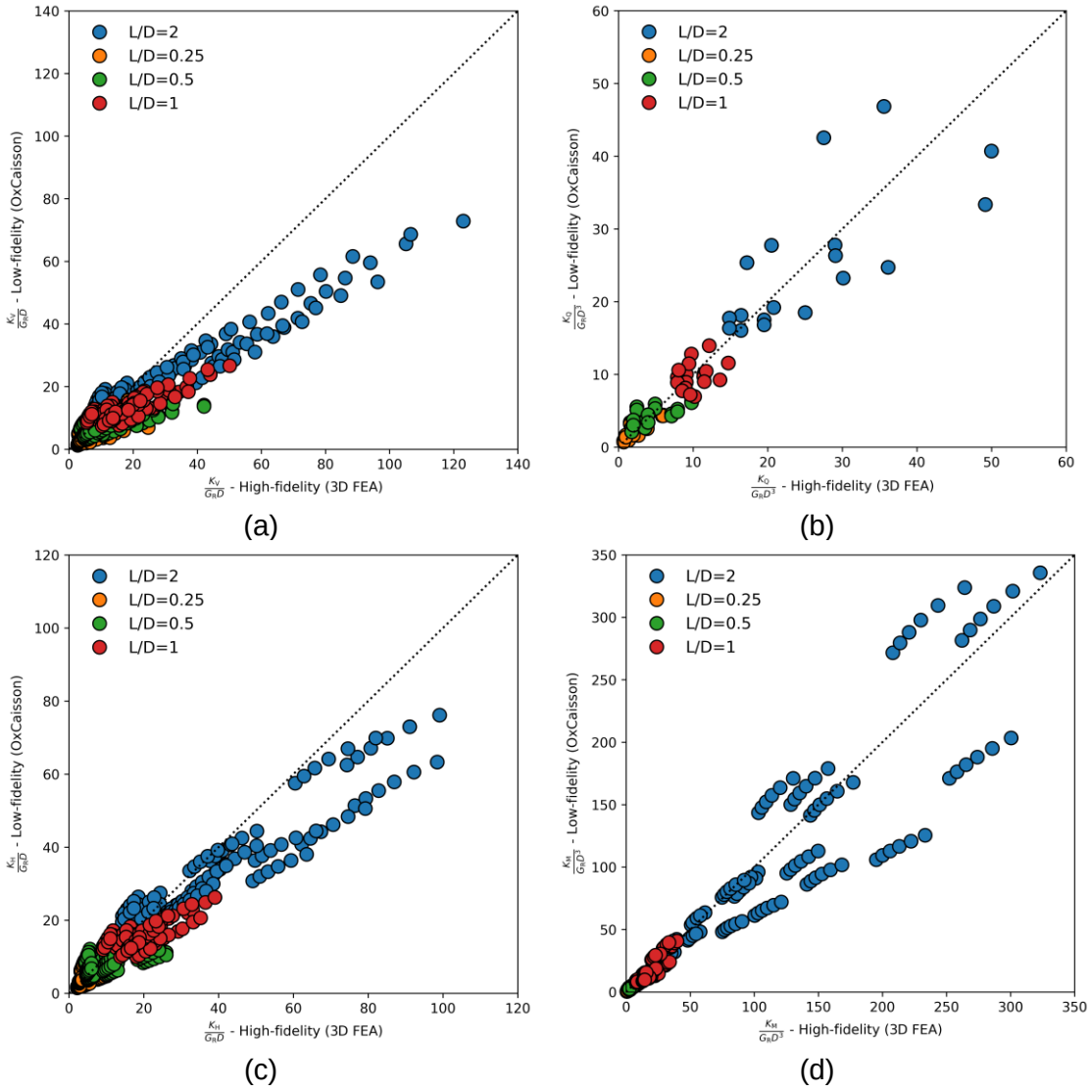

Figure 4 Relationships between the high-fidelity data generated by 3D FEA and the corresponding low-fidelity data generated by OxCaisson for the normalized (a) vertical, (b) torsional, (c) horizontal, and (d) moment stiffness of a suction caisson for all the layered soil profiles considered in this study.

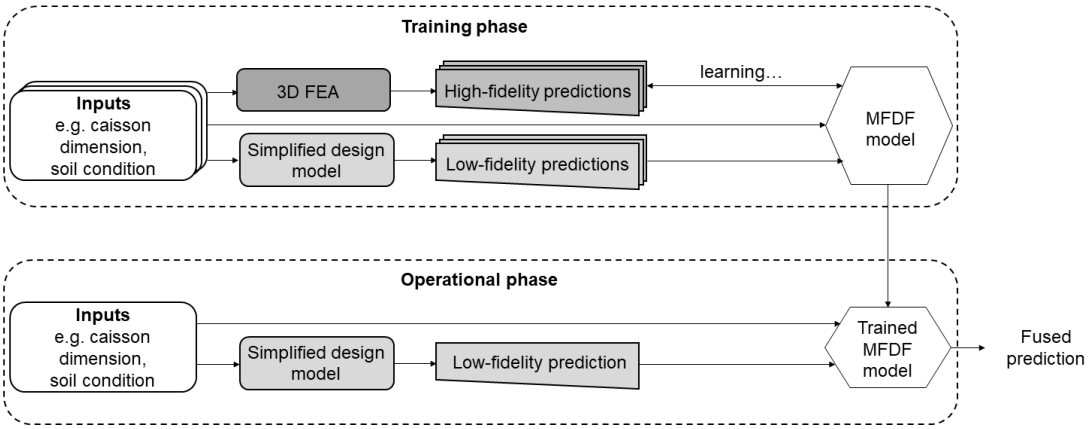

Figure 5 Schematic diagram summarizing the training and operational phases of the MFDF model.

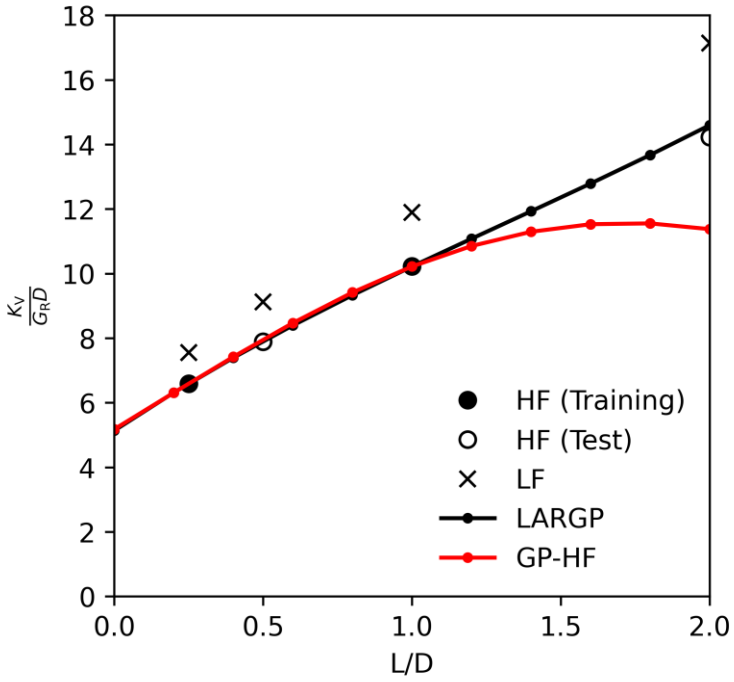

Figure 6 Comparison of high-fidelity (HF) data (calculated using 3D FEA) for the normalized vertical stiffness of a suction caisson embedded in a specific layered soil configuration (Case P2 of Table 1 for $\alpha = 0$) and the corresponding low-fidelity (LF) data (calculated using OxCaisson). The mean predictions of LARGP and GP-HF are also shown.

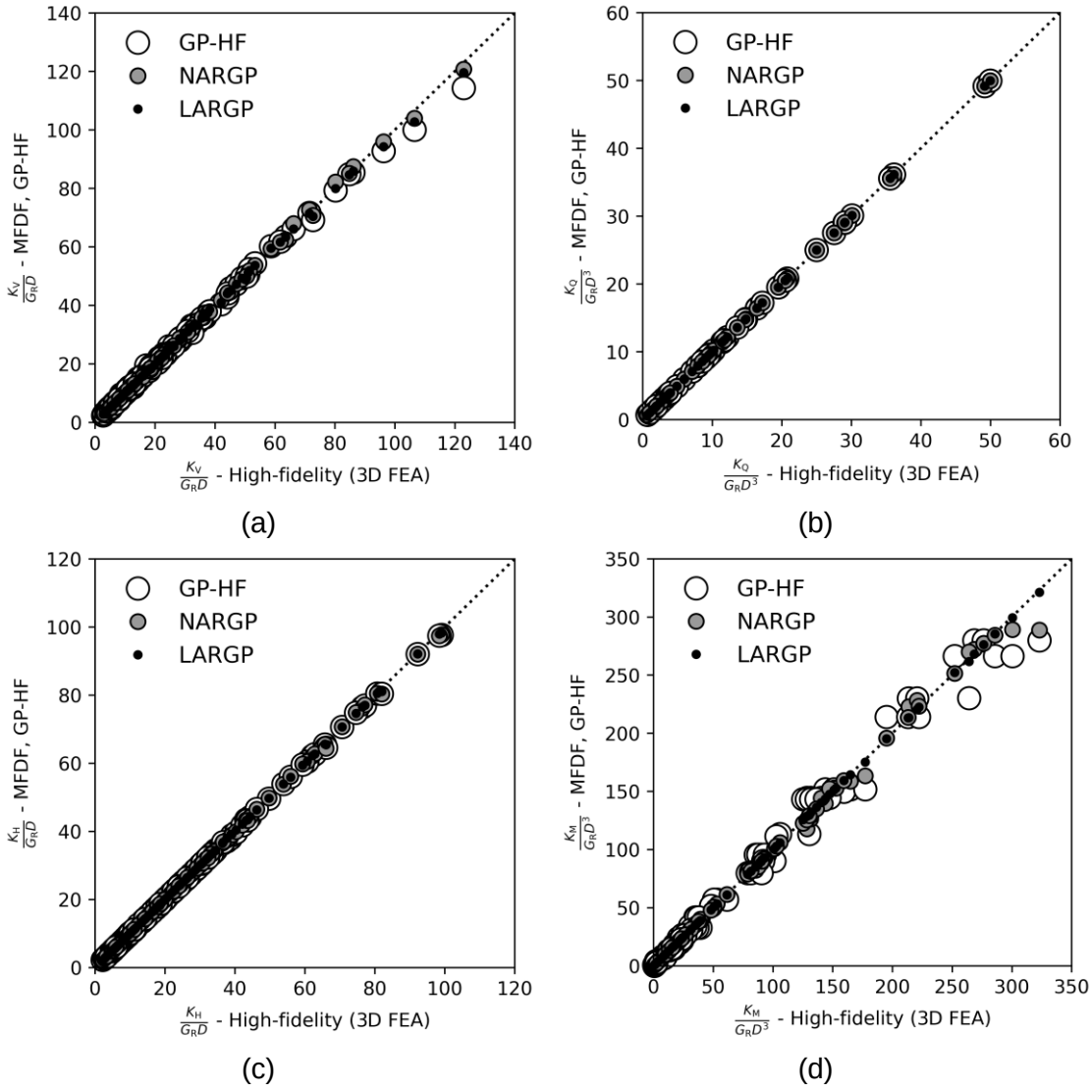

Figure 7 Comparison of high-fidelity data (calculated using 3D FEA) for the normalized (a) vertical, (b) torsional, (c) horizontal, and (d) moment stiffness of a suction caisson for all the layered soil profiles considered in this study with the corresponding predictions by the MFDF models (LARGP and NARGP) and the single-fidelity machine learning model (GP-HF) for the training dataset TD60.

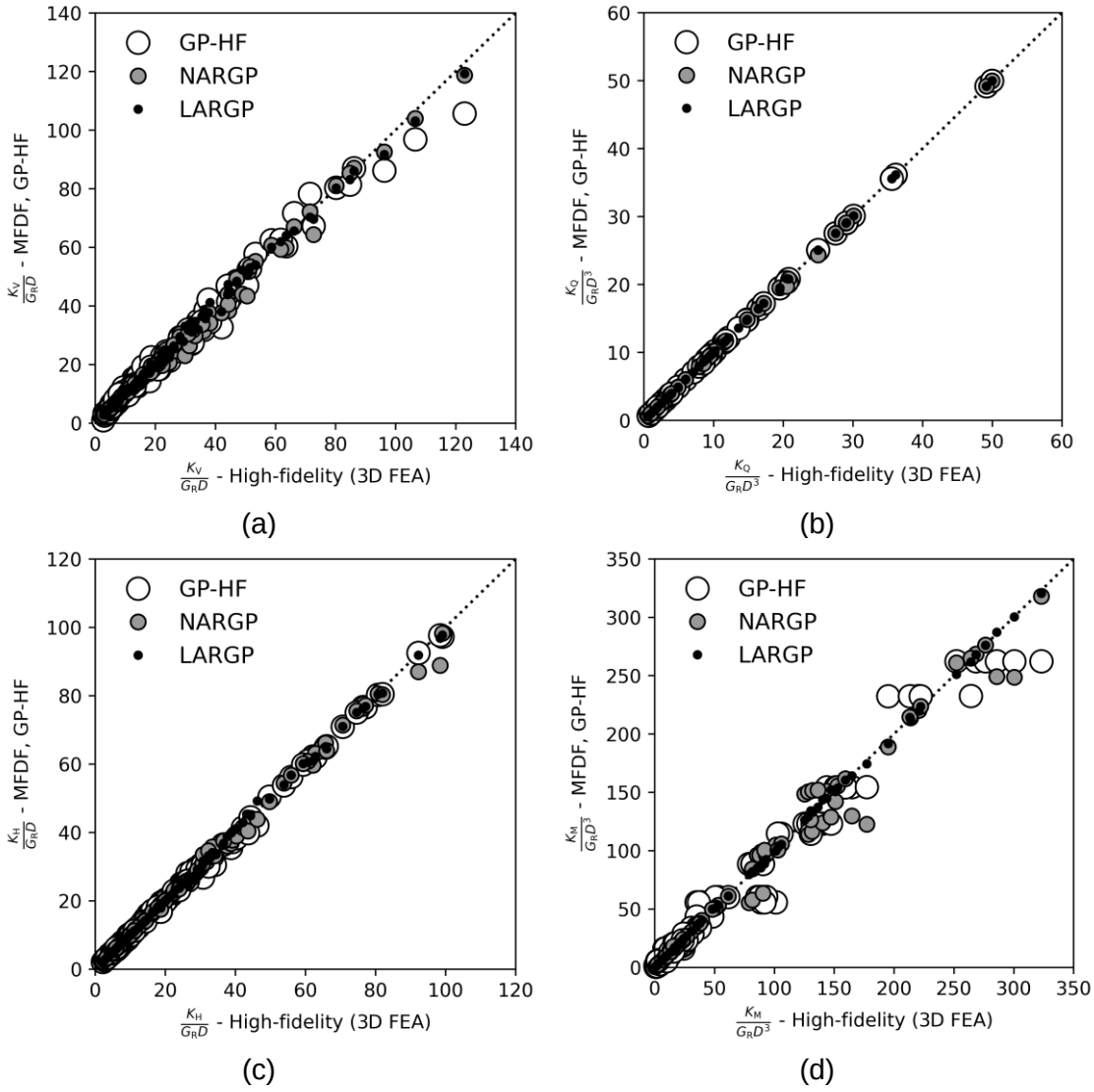

Figure 8 Comparison of high-fidelity (HF) data (calculated using 3D FEA) for the normalized (a) vertical, (b) torsional, (c) horizontal, and (d) moment stiffness of a suction caisson for all the layered soil profiles considered in this study with the corresponding predictions by the MFDF models (LARGP and NARGP) and the single-fidelity machine learning model (GP-HF) for the training dataset TD30.

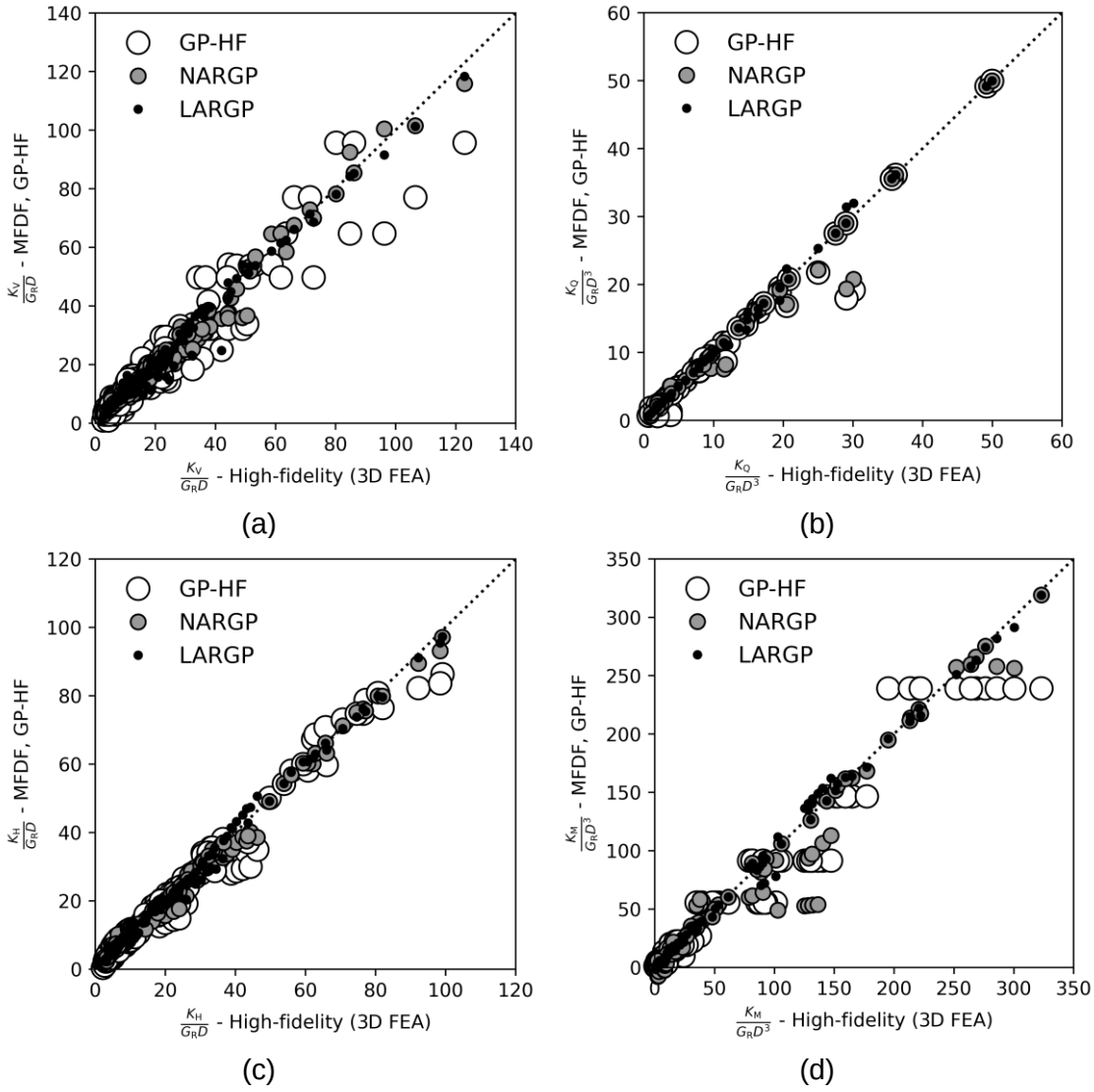

Figure 9 Comparison of high-fidelity (HF) data (calculated using 3D FEA) for the normalized (a) vertical, (b) torsional, (c) horizontal, and (d) moment stiffness of a suction caisson for all the layered soil profiles considered in this study with the corresponding predictions by the MFDF models (LARGP and NARGP) and the single-fidelity machine learning model (GP-HF) for the training dataset TD15.

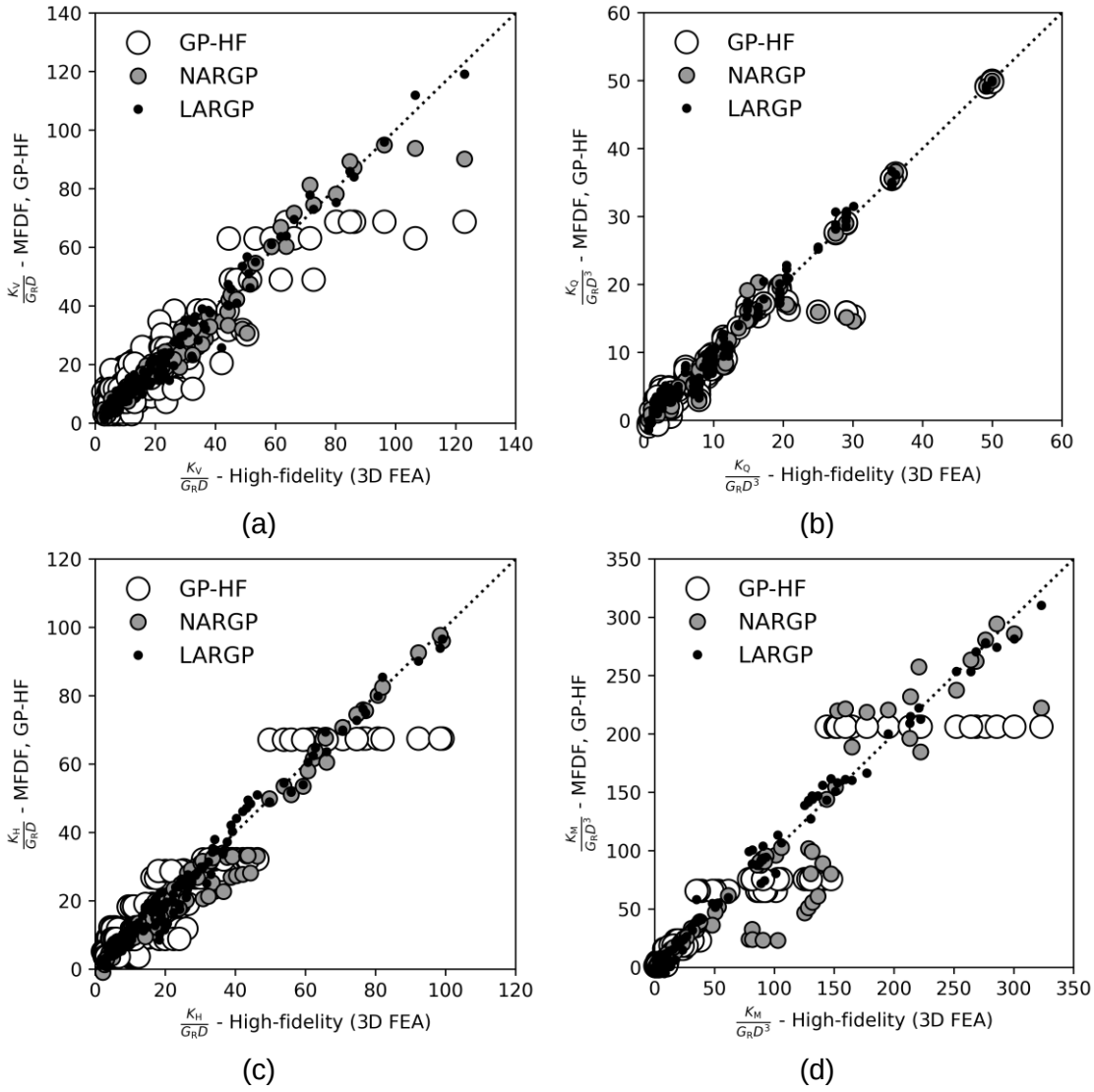

Figure 10 Comparison of high-fidelity (HF) data (calculated using 3D FEA) for the normalized (a) vertical, (b) torsional, (c) horizontal, and (d) moment stiffness of a suction caisson for all the layered soil profiles considered in this study with the corresponding predictions by the MFDF models (LARGP and NARGP) and the single-fidelity machine learning model (GP-HF) for the training dataset TD7.

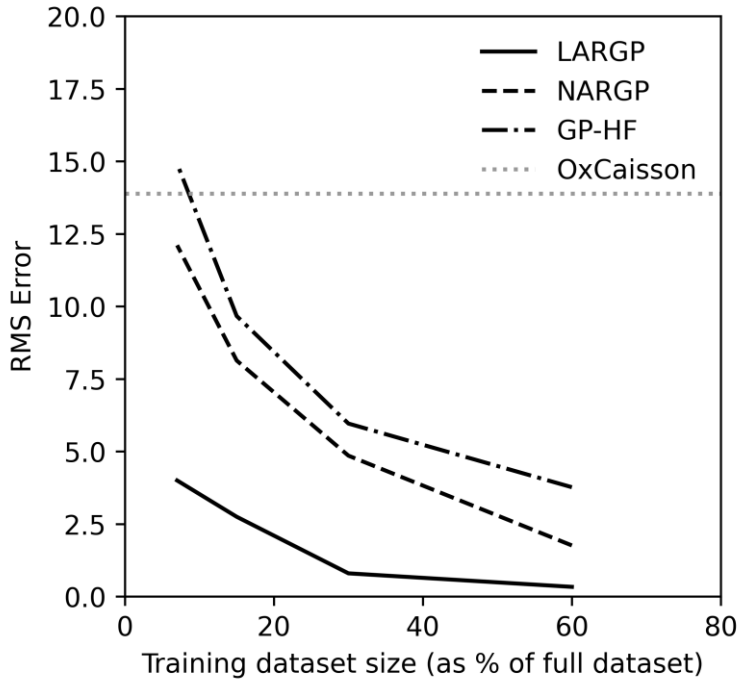

(a)

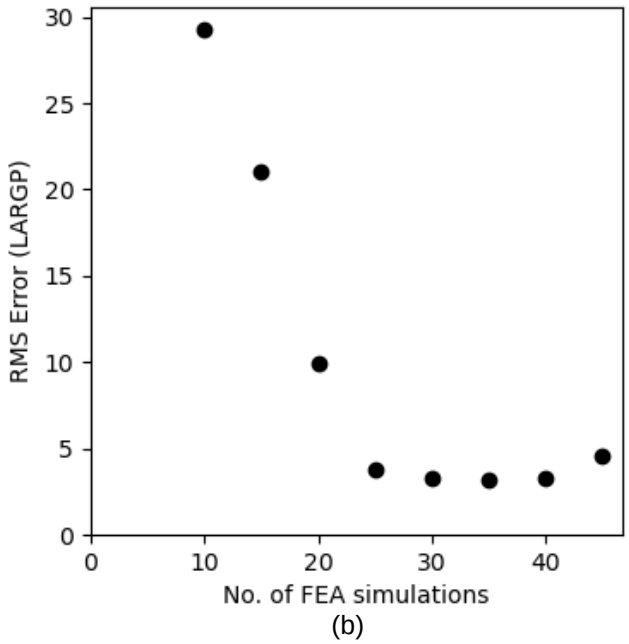

(b)

Figure 11 (a) Influence of the training data size (as a percentage of the full high-fidelity dataset) on the RMS errors for the various models. (b) RMS error for LARGP stabilizes at around 35 FEA simulations.

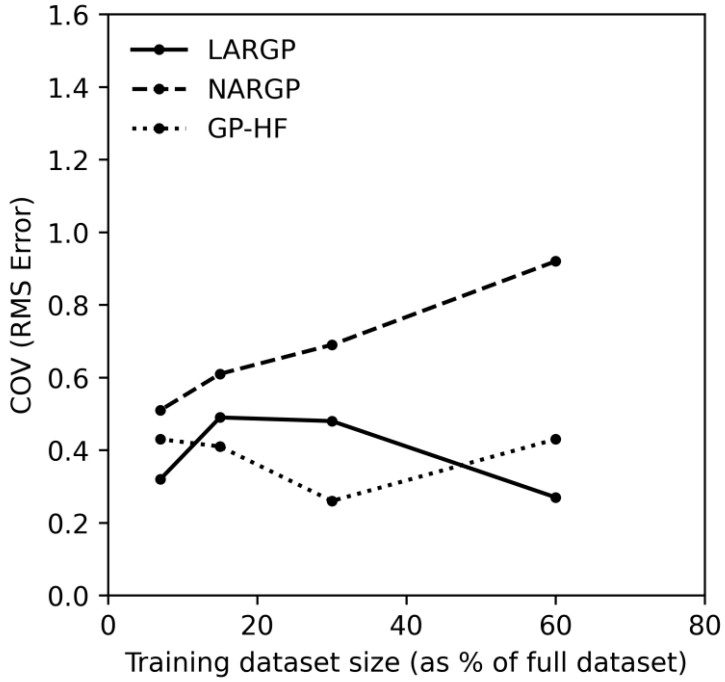

Figure 12 Influence of the training data size (as a percentage of the full high-fidelity dataset) on the COV of the RMS errors for the various models, given 20 random samplings of the training and test datasets.

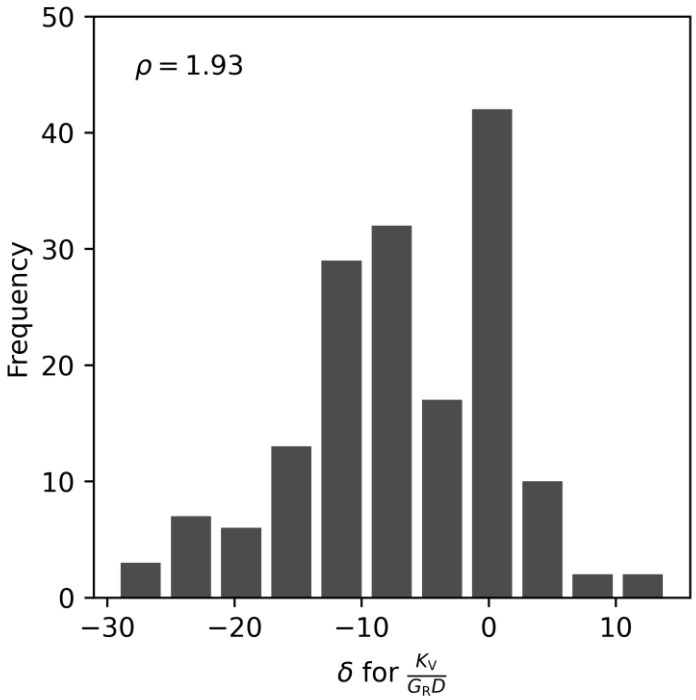

Figure 13 The trained scale factor ρ and a histogram of the trained offset factors δ of LARGP for predicting the normalized vertical stiffness of the caisson in Fig. 7a. The scale factor is constant, while the offset factor may vary for each input.